6

Exploration in Detector Simulation & Intrumentation

Detector simulation and instrumentation play a paramount role in the realm of particle physics, enabling the exploration of the fundamental building blocks of the universe. Through meticulous simulation of particle interactions within detectors, scientists can unravel the complex behaviors of subatomic particles, shedding light on the underlying principles that govern the universe's structure and behavior. Cutting-edge instrumentation designs are equally pivotal, as they provide the tools to capture and measure these elusive particles with unprecedented precision. By meticulously simulating and innovatively engineering detection systems, researchers can decipher the enigmatic particles' properties, interactions, and decay processes, ultimately advancing our understanding of the cosmos and paving the way for breakthroughs in both theoretical physics and real-world applications.

6.1   Overview of the work

In the following chapter, I will delve into the extensive research and development conducted throughout my doctoral journey, focusing on detector simulation and instrumentation. This chapter is thoughtfully structured into two distinct sections, each dedicated to a specific aspect of my work.

The initial section is dedicated to the simulation work, where I have invested significant effort in investigating the detector sensitivity of the Hyper Kamiokande (HK) detector, particularly in the presence of radioactive background noise. This exploration is pivotal in enhancing our understanding of the detector's capabilities in real-world scenarios, where radioactive interference can pose significant challenges. Furthermore, within this section, we delve into the exciting realm of supernova neutrino detection, elucidating how the HK detector's sensitivity can contribute to our comprehension of these elusive cosmic events. This entails a thorough examination of the detector's performance and its potential to detect supernova neutrinos, shedding light on a fascinating area of astrophysics.

The later part of this chapter is dedicated to instrumentation, where my primary focus revolved around the fabrication and subsequent characterization of resistive plate chamber detectors. This endeavor is instrumental in advancing detector technology, as these resistive plate chamber detectors play a crucial role in particle physics experiments. Through meticulous experimentation and analysis, I aimed to optimize their design, functionality, and performance characteristics. This instrumentation work serves as an essential building block, not only for my research but also for the broader field of experimental physics, as it contributes to the refinement of detection instruments used in various scientific investigations.

6.2   HK Background simulation

This section outlines a comprehensive framework for our endeavors in detector simulation work. We also highlight our interesting results in the following subsections. For the detector simulation work, we will consider primarily the proposed Hyper Kamiokande (HK) detector in Japan. For the simulation studies, the GEANT4 and WCSim packages will be used. GEANT4 is a commonly used simulation toolkit for simulating the passage of particles through matter. WCSim is a very flexible GEANT4-based program for developing and simulating large WC detectors. The HK collaboration extensively uses the WCSim package for the detector simulation. The detector geometry of WCSim

consists of top and side photo-multiplier tubes (PMTs). Provided the basic parameters of the detector, it automatically lays out the PMTs on the walls of the detector. These two packages will be used often for performing the simulation studies.

The presence of gamma-ray background radiation has the potential to exert an influence on the sensitivity of the Hyper Kamiokande detector when it operates at lower energy levels. In the scope of our research, we have undertaken the task of analyzing the gamma-ray spectrum associated with this background radiation. Our gratitude extends to the collaborative efforts of individuals such as Takatomi Yano and Itaru Shimizu, who have graciously provided us with the data file containing crucial information pertaining to the background. This data file is a comprehensive repository of details concerning the abundance of isotopes as well as the energy spectrum associated with these isotopes. To visually represent this valuable dataset, we have generated a plot that serves as a graphical representation of its contents. In this plot, the X-axis is dedicated to Energy, while the Y-axis is used to display the Probability of gamma emission. To distinguish between various isotopes within the dataset, we have employed a color-coded scheme, with each distinct color denoting a different isotope.
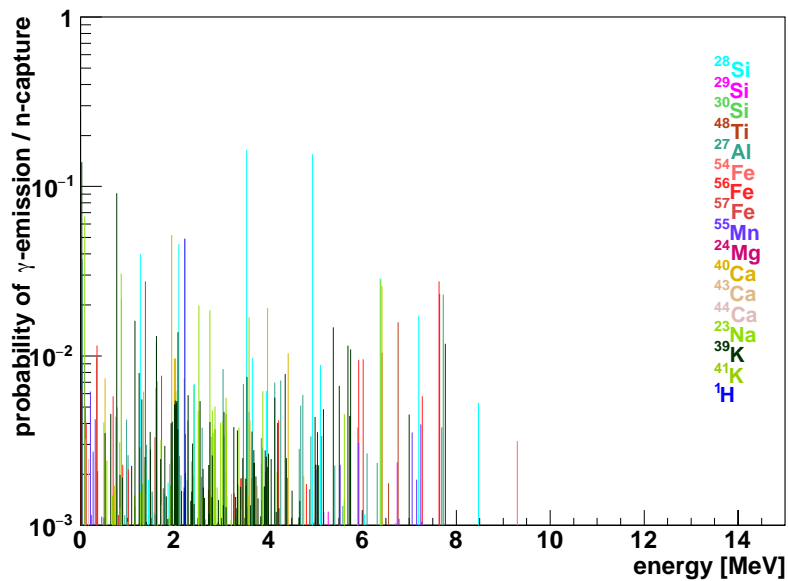

FIGURE 6.1: Gamma ray background at the Hyper Kamiokande detector.

This analysis and visualization of the gamma-ray background data is essential for gaining a deeper understanding of its characteristics and its potential impact on the performance of the Hyper Kamiokande detector at lower energy levels.
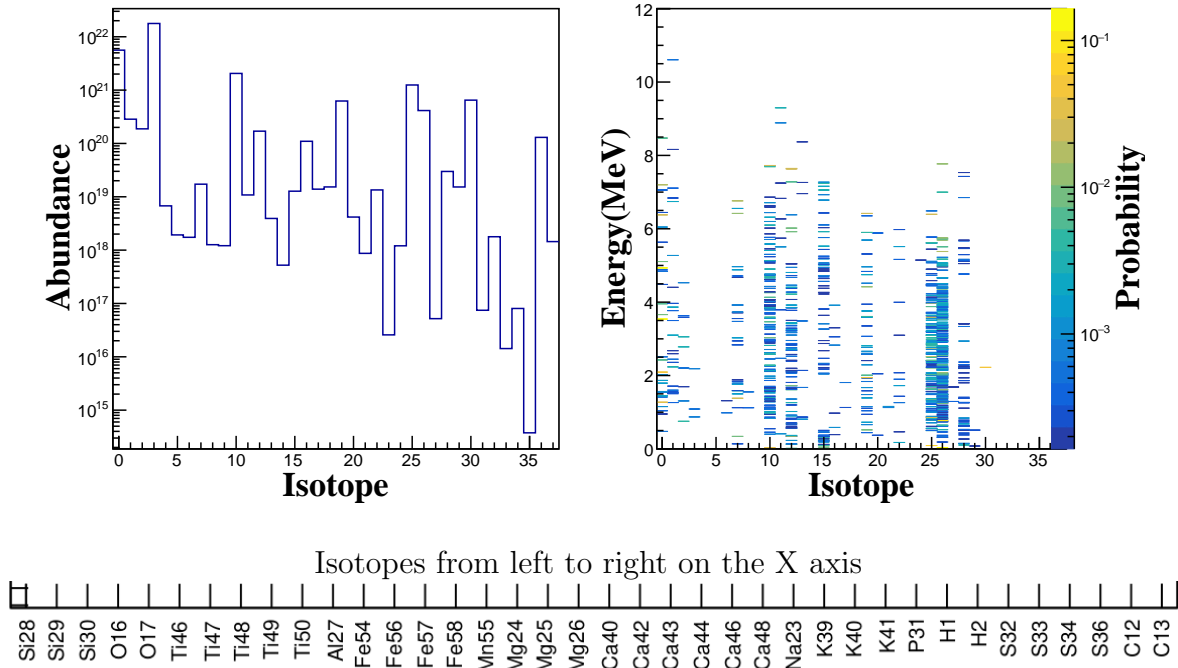
FIGURE 6.2: Gamma Ray Spectrum for the Hyper Kamiokande detector. *Left:* Abundance distribution of isotopes, *Right:* Energy distribution of the isotopes.

We have generated the following plots based on the data file at our disposal. The first plot, situated on the left side, illustrates the relationship between Abundance and Isotope. Meanwhile, on the right side, we have depicted a three-dimensional plot showcasing the interplay between Isotope, Energy, and Probability. It is worth noting that the lower panel presented below is essentially a magnified view of the X-axis labels, which are synchronized across both plots, running from left to right. In an effort to maintain consistency, we have arranged the isotopes in accordance with this left-to-right progression.

6.2.1 Detector Simulation Procedure

Turning our attention to the simulation aspect, it's essential to acknowledge that the gamma background is influenced by two critical factors: the relative abundance of isotopes and their respective energy spectra. In our simulation methodology, we have thoughtfully integrated both abundance and energy spectrum information to provide a comprehensive representation of the gamma background. To accomplish this, we follow a systematic procedure. Initially, we start by selecting an isotope from the available options. This selection is made by generating a random number, which is proportional to the isotope's abundance. This information is derived from the Abundance vs. Isotope

plot, as shown in the preceding slide. By employing this method, we ensure that the chosen isotope reflects the real-world scenario accurately.

Once we have identified the isotope, the next step is to determine the energy of the emitted gamma rays. This energy is directly associated with the gamma energy spectrum characteristic of that particular isotope. It's crucial to capture this energy spectrum accurately, as it plays a pivotal role in the subsequent stages of our simulation. With the energy of the gamma rays established, we proceed to simulate their behavior within the rock structure. This entails defining their position and direction, taking into consideration the permissible ranges as dictated by the geological characteristics of the rock material. In essence, our simulation process incorporates both isotopic abundance and energy spectrum information, enabling us to generate a realistic representation of the gamma background. This multi-step approach ensures that our simulations align closely with real-world conditions, making them a valuable tool for understanding and analyzing gamma radiation scenarios.

We are now ready to put our discussed simulation methodology into practice by utilizing a simplified model. Specifically, we have chosen to employ the fundamental B1 example provided by GEANT4 as the foundation for our simulation investigation. In order to simulate gamma particles, we have employed the methodology elucidated in the preceding slide, and this has been incorporated into the PrimaryGeneratorAction class. The outcome of our simulation effort encompasses both the simulated energy data and isotope information. This comprehensive dataset is retained in the output for the express purpose of cross-referencing our results with the initial data contained within the input file. This validation process serves as a crucial step in assessing the accuracy and fidelity of our simulation model against the real-world data it seeks to emulate.

6.2.2   Abundance Distribution

We conducted simulations across a range of statistical parameters to investigate their impact on our results. The following quartet of graphs illustrates a comparative analysis between the original input data and the simulated output data. Specifically, we have charted the relationship between Abundance and Isotope for varying numbers of events.

In these visual representations, the blue histogram represents the input data, while the red histogram corresponds to the simulated output generated through our modeling process. Through our observations, we discerned a notable trend: as we increment the statistical parameters, there is a discernible enhancement in the alignment between the simulated results and the input data. This phenomenon underscores the significance of statistical considerations in improving the fidelity of our simulations.
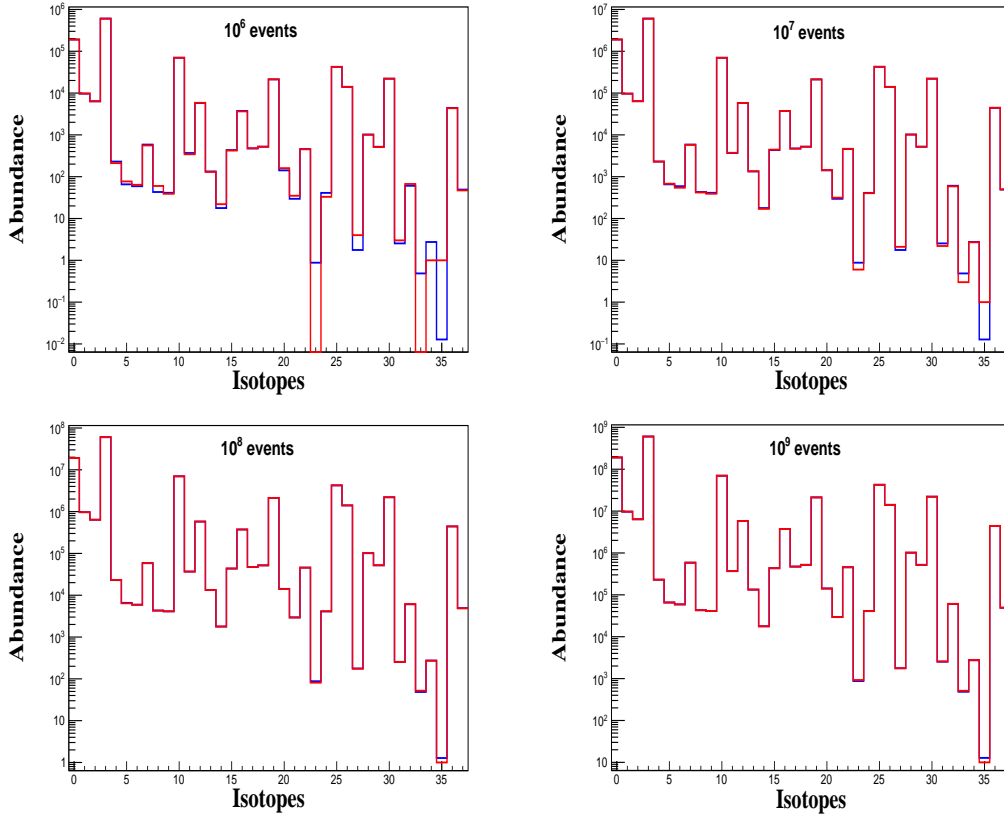
FIGURE 6.3: Abundance distribution of the isotopes for the given (blue histogram) and the simulated (red histogram) output for various statistics.

6.2.3 Energy Distribution

Next, we performed an examination of the energy spectrum data in our analysis. In this section, we present the outcomes specifically for the Si29 isotope, utilizing a dataset comprising 10^6 events as shown in figure 6.4. The figure consists of two spectra: the left plot illustrates the initial energy spectrum extracted from the data file, while the right plot displays the energy spectrum generated by the simulation. The left plot essentially portrays the energy spectrum as it was originally obtained from the data file, serving as a reference point for our analysis. In contrast, the right plot showcases the output energy spectrum derived from the simulation process, which allows us to compare and evaluate how closely the simulation matches the actual data. This comparative analysis is crucial for validating the accuracy and reliability of our simulation methodology in reproducing the observed energy distribution for the Si29 isotope in the specified event count of 10^6.

To assess the energy spectrum output in comparison to the input, we have performed a normalization procedure by scaling the input histogram with respect to the output

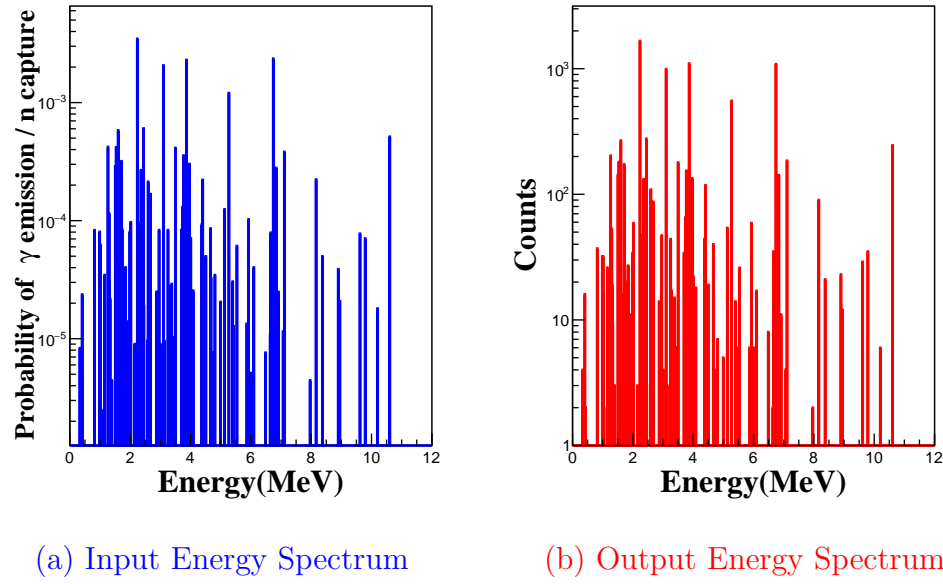(a) Input Energy Spectrum · · · · · · · · (b) Output Energy Spectrum

FIGURE 6.4: Energy distribution of the isotope for the given (left) and simulated (right) result.

histogram and subsequently calculating the ratio between the two. The figure 6.5 illustrates this analysis, where the X-axis corresponds to energy values, and the Y-axis represents the histogram ratio. The ratio of the input and output energy histogram is performed after scaling of the input histogram.

$$R = \frac{Output\ Energy\ Spectrum}{Input\ Energy\ Spectrum}$$

.

Similarly, we have conducted a parallel analysis for varying numbers of events, specifically for 10^6, 10^7, 10^8 and 10^9 as shown in figure 6.5. This work offers a concise overview of energy spectrum analysis across varying numbers of statistical data points. The key observation here is that as the quantity of statistical data points increases, the ratio approaches unity. In simpler terms, this indicates a high degree of conformity between our simulation results and the input data information. It's important to note that this analysis is specifically demonstrated for the Si29 isotope, but similar assessments have been conducted for other isotopes with consistent findings. In essence, as we increase the number of statistical data points, the degree of alignment between our results and the actual data consistently improves.
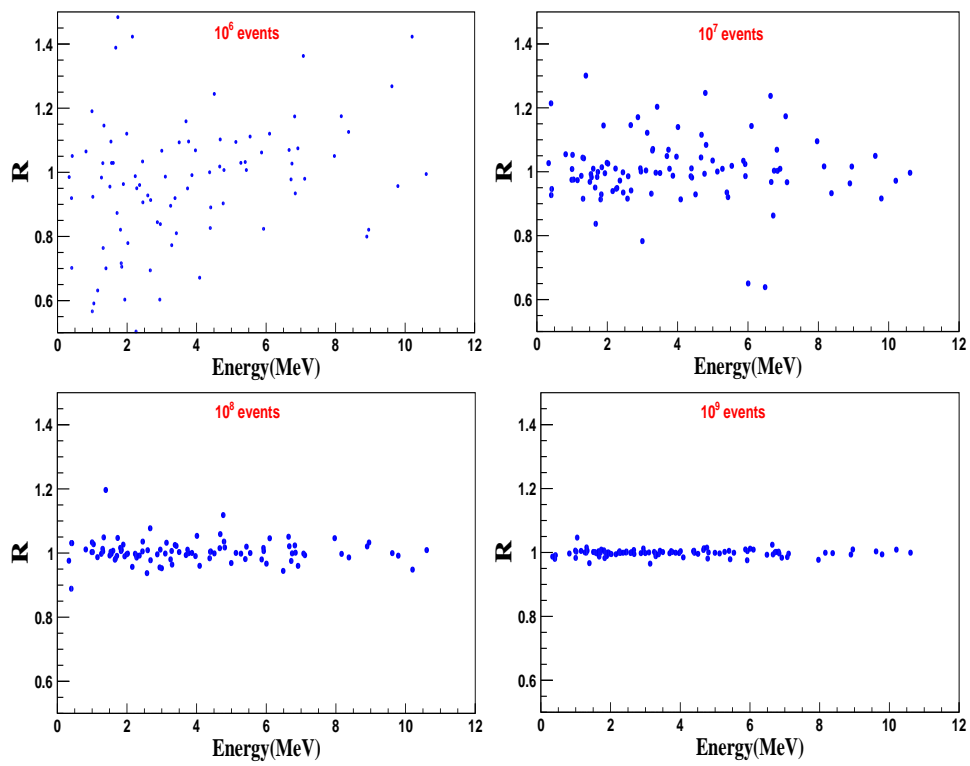
FIGURE 6.5: Ratio of isotope energy spectrum as a function of input energy for different statistics.

6.3   Probing neutrino mass ordering at HK

The discovery of neutrino oscillations at the Super-Kamiokande (SK) and Sudbury Neutrino Observatory (SNO) has firmly established the existence of neutrino mass. This revelation led to the formulation of three neutrino mass eigenstates (ν_1, ν_2, ν_3), associated with the masses (m_1, m_2, m_3). Neutrino oscillation theory reveals that the flavor eigenstates (ν_e, ν_μ, ν_τ) are linear combinations of these mass eigenstates, governed by a 3x3 unitary matrix known as the PMNS matrix (Pontecorvo, Maki, Nakagawa, and Sakata), characterized by three mixing angles (θ_{13}, θ_{23}, θ_{12}) and a CP phase (δ_{CP}). While θ_{12} has been measured and found to be approximately $\sin^2\theta_{12} = 0.30$, θ_{23} and δ_{CP} remain poorly constrained. Notably, θ_{13} is observed to be very small. Furthermore, the absolute masses of neutrinos are still unknown because neutrino oscillations enable the measurement of only the squared mass differences, denoted as $\Delta m_{ij}^2 = m_i^2 - m_j^2$, where i and j can be 1, 2, or 3. Δm_{12}^2 (also known as Δm_{sol}^2) has been measured from solar neutrino data and falls in the range of $[7.03, 8.09] \times 10^{-5} \ eV^2$. The remaining mass squared differences, collectively referred to as Δm_{atm}^2 (or Δm_{31}^2, Δm_{32}^2), obtained from atmospheric neutrino data, do not provide information on the sign (positive or negative) of Δm_{atm}^2, leading to the "mass ordering" or "mass hierarchy" problem. Two possible scenarios arise Normal Ordering (NO) where $m_1 < m_2 < m_3$, and Inverted Ordering (IO) where $m_3 < m_1 < m_2$. Other possibilities, such as no hierarchy, are not definitively ruled out.

Resolving these issues requires a multifaceted approach involving various experiments and diverse sources of neutrinos. Solar and atmospheric neutrinos have already contributed substantial insights. Beyond terrestrial sources, astrophysical neutrino sources, both galactic and extragalactic, could be pivotal. These sources emit neutrinos spanning a wide energy range, from MeV to PeV, encompassing phenomena like supernovae, gamma-ray bursts, and more. To detect such neutrinos, a range of current and upcoming detectors exists, including SK, JUNO, Hyper-Kamiokande (HK), DUNE, and high-energy detectors like IceCube, IceCube-Gen2, and KM3NeT. A supernova explosion in our Milky Way galaxy holds the potential to provide extensive information, not only about neutrinos but also the physics of such cataclysmic events. These supernovae can produce an immense number of MeV neutrinos, around 10^{58}, carrying the majority of the star's gravitational energy. While past observations, such as those from SN 1987A in the Large Magellanic Cloud, detected a limited number of neutrinos (approximately 25-30 events), future galactic supernovae are anticipated. With a typical rate of 1-2 per century, we may witness one soon. However, our understanding of neutrino emission from supernovae relies on computer simulations due to the distances of

observed supernovae (beyond 10 Mpc). Electromagnetic emissions, detected by X-ray or radio telescopes, originate from the outer regions and offer limited information about the core. In contrast, neutrinos, being weakly interacting, can escape easily and convey core information. These simulations, predominantly 1D and 2D due to computational constraints, provide crucial neutrino data for analysis.

These simulations reveal distinct spectra for different neutrino flavors due to various production mechanisms and interactions. For instance, electron neutrinos (ν_e) exhibit a significant initial spike in their spectra known as the "neutronization burst" due to high electron degeneracy in the core. Electron anti-neutrinos ($\bar{\nu}_e$) and heavy leptonic neutrinos (ν_μ, ν_τ, collectively referred to as ν_x), have different production mechanisms and similar interactions. The spectra of ν_x rise faster than that of $\bar{\nu}_e$. The shock-wave resulting from core bounce, crucial for the supernova explosion, loses energy through neutrino emission, leading to the shock stalling and an accretion phase. During the accretion phase, neutrinos are trapped in the core and transfer energy to the shock, potentially reviving it. The subsequent explosion reduces matter density, enabling neutrinos to diffuse out during the "cooling" phase. All flavors are produced nearly equally during this phase. If the shock fails to revive, a black hole may form, resulting in a sudden drop in neutrino flux. Neutrinos produced deep in the core undergo flavor conversion (Mikheyev-Smirnov-Wolfenstein, MSW effect) due to interactions with dense matter, resulting in different flavor fluxes for NO and IO. Detecting these differences in neutrino flux from a galactic supernova could elucidate the mass ordering. Presently, SK can detect approximately 7,000 neutrinos from a galactic supernova, while the larger HK, along with JUNO and DUNE, will provide even greater capabilities. DUNE focuses on detecting the ν_e burst (neutronization burst), while HK and JUNO target the rise in ν_x, which is reflected in the $\bar{\nu}_e$ flux due to oscillation.

In this study, we analyze data from simulations conducted by Garching and Nakazato to explore the potential of these future detectors, DUNE, HK, and JUNO, in resolving the neutrino mass ordering. Our statistical analysis employs the Kolmogorov-Smirnov (KS) statistics, and we find significant distinctions between the two mass ordering scenarios for all detectors.

6.3.1 Details of Garching supernova model

Simulating core-collapse supernovae (CCSN) realistically necessitates a three-dimensional framework and substantial computing power, a feat currently unattainable. Consequently, extant CCSN simulations in the literature rely on hydrodynamic codes founded
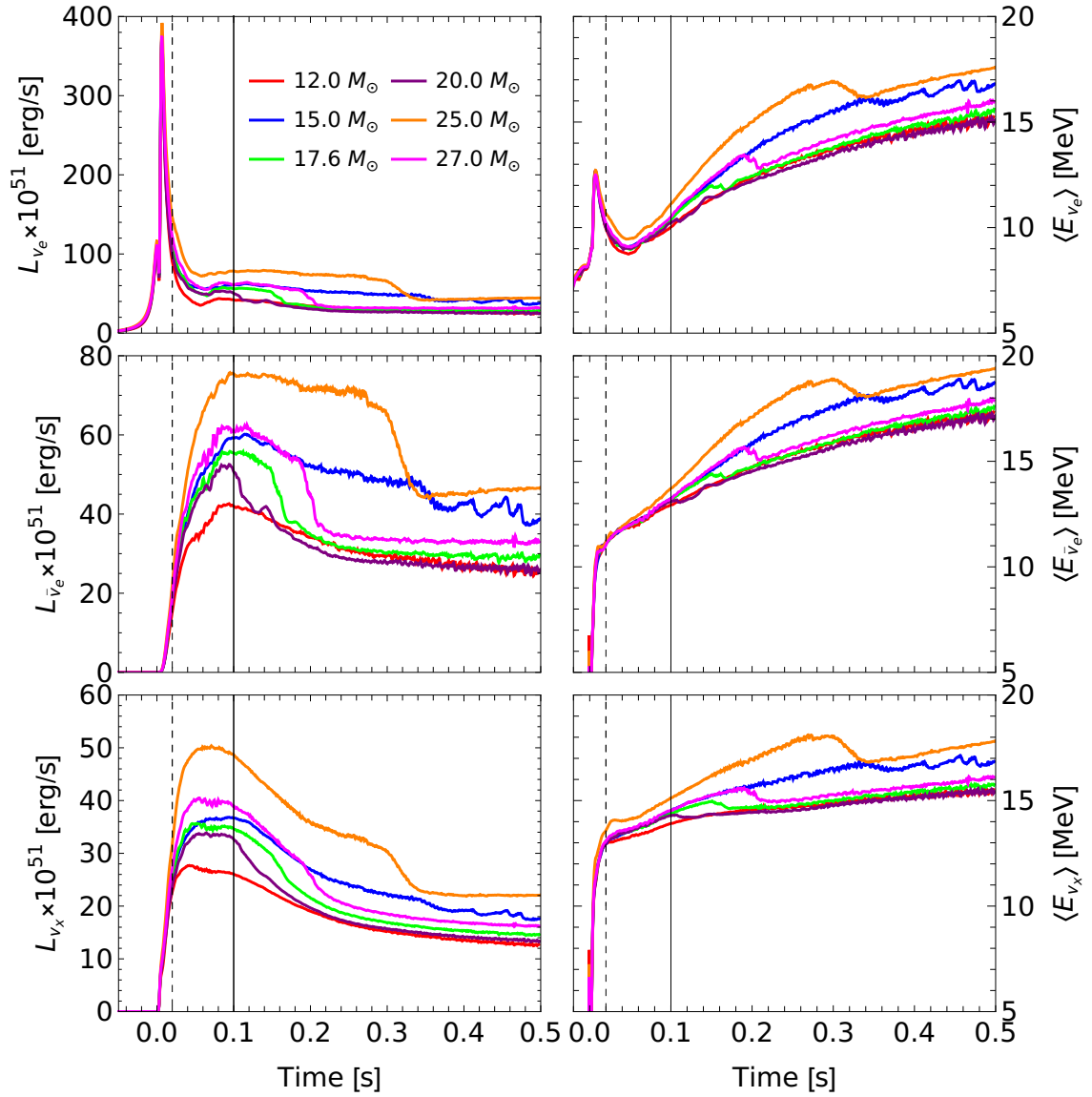
FIGURE 6.6: The figure displays the luminosities (on the left) and average energies (on the right) of various neutrino types released in simulations of Core-Collapse Supernovae (CCSNe) originating from distinct progenitor masses [cite]. The upper panel presents data for electron neutrinos, while the middle panel pertains to electron anti-neutrinos. Neutrinos and anti-neutrinos of muon and tau flavors are treated as indistinguishable entities and are collectively labeled as $\nu_{\rm x}$, as depicted in the lower panel. To highlight specific time points of interest, vertical dashed and solid lines are included at 20 ms and 100 ms, respectively.

on simplified assumptions to address the equation of state, with these assumptions varying across different simulation models. Consequently, distinct characteristic features are exhibited in the neutrino fluxes of various simulated models. In this section, we present a concise overview of the CCSN simulation from Garching [197, 198], which forms the

basis of our analysis. The Garching model simulation utilizes the PROMETHEUS-VERTEX code [199, 200] to solve the hydrodynamic equations of states for neutrino number, energy, and momentum moments of $\mathcal{O}(v/c)$, incorporating a variable Eddington factor closure [201]. Employing the "ray-by-ray plus" method to consider two and three-dimensional effects, assuming azimuthal symmetry around the radial direction, the simulation adopts a Newtonian hydrodynamic treatment with a reasonable correction to the gravitational potential for approximate general relativistic effects. This simulation employs three distinct equations of state (EOS): Lattimer and Swesty with nuclear incompressibility of 220 MeV, Shen EOS, and SFHo hadronic EOS [202]. The analysis focuses on results obtained using the Lattimer and Swesty EOS for six different progenitor mass models, yielding neutrino luminosity, average energy, and average squared energy as functions of time. The luminosities and average energies of various neutrino species for these models are depicted in figure 6.6.

6.3.2 Signatures of supernova neutrino emission

Hydrostatic burning of nuclear fuel within a star leads to the formation of a degenerate iron or oxygen-neon-magnesium core, which subsequently undergoes collapse due to strong gravitational forces [203]. This collapse results in the generation of an extensive quantity of MeV neutrinos, on the order of $\mathcal{O}(10^{58})$, within a few seconds, potentially accompanied by a supernova explosion. The star may ultimately transform into a compact object, such as a black hole or neutron star. The initial few hundred milliseconds of neutrino emission carry vital information about neutrino mixing [204]. These neutrinos undergo flavor conversion due to the Mikheyev-Smirnov-Wolfenstien (MSW) effect as they traverse the extremely dense core towards the stellar surface. Furthermore, the neutrino emission during the first 100 milliseconds occurs in two distinct phases: the "neutronization burst phase" (lasting about 25 milliseconds during collapse) and the "accretion phase" (continuing for approximately a second, with our focus limited to about 100 milliseconds due to unique flavor distinguishing features). In the subsequent discussion, we elaborate on these neutrino emission processes, their flavor conversion, and potential applications in probing neutrino mass ordering.

Neutronization Burst: The collapse of a massive star, depleted of nuclear fuel, results in an extremely dense core (around 10^{14} gcm^{-3}) that rebounds, creating a powerful shock propagating radially outward through the dense matter. This core bounce prompts a burst of electron neutrinos (ν_e), generated by electron capture on protons. Termed the "neutronization burst," this phenomenon involves the conversion of most protons into

neutrons (deleptonization). The burst occurs when the shock reaches a low enough density (the neutrino sphere) for neutrinos to escape, lasting approximately 20-30 milliseconds from the onset of core bounce (duration may vary among different simulation models). Electron anti-neutrinos ($\bar{\nu}_e$) and heavy lepton flavors (ν_x) can be produced through electron-positron pair annihilation and nucleon-nucleon bremsstrahlung. Although $\bar{\nu}_e$ can also be created by positron capture on neutrons, the production of electron anti-neutrinos and heavy lepton flavors (mu and tau) is suppressed during this phase due to high electron degeneracy in the core. As a result, the neutrino luminosity of the neutronization burst is predominantly characterized by a sharp peak in the ν_e spectra, as illustrated in figure 6.6. The right panel depicts the average energies of these neutrinos over time. The neutronization burst is evident as a peak in the energies of ν_e (top right), reflecting the sudden temperature rise and subsequent fall during the core collapse. Both the luminosity and average energy of ν_e decrease rapidly after the prompt burst until deleptonization saturates, resulting in an extremely neutron-rich core.

Accretion phase: Following the completion of neutrino sphere deleptonization, the production of mu and tau neutrinos (anti-neutrinos), ν_x, initiates due to the elevated temperature of the matter behind the shock. These neutrinos are generated through electron-positron pair annihilation and nucleon-nucleon bremsstrahlung, processes that become efficient with increasing temperature. As $\bar{\nu}_e$ becomes sufficiently dense, neutrino-anti-neutrino pair annihilation also contributes to ν_x production ($\nu_e \bar{\nu} e \longrightarrow 2\nu x$). This results in a sharp increase in the ν_x luminosity, contrasting with the slower rise of $\bar{\nu} e$. The faster rise of νx luminosity compared to $\bar{\nu}_e$ is a consistent feature observed in various CCSN simulation models, as illustrated in figure 6.6 and references. The luminosities of these neutrino flavors reach their maxima at approximately 100 milliseconds. The extensive neutrino emission and the interaction of the shock with dense matter lead to a slowdown of the shock, inducing the accretion of matter behind it. In the case of a successful explosion, the shock is revived due to energy deposition by neutrinos to the matter behind the shock, resulting from neutrino-matter interactions. Consequently, the neutrino luminosity experiences a substantial decrease, reflecting the shock revival. In scenarios where a black hole forms during the collapse, the shock fails to rejuvenate, leading to a sharp decline in neutrino luminosities. It's worth noting that the shock revival time may depend on the progenitor mass. The average energy of ν_x generally surpasses that of electron-flavored neutrinos. This is because ν_x decouples from matter at a smaller radius, separating earlier, as they lack sufficient energies to initiate charge current interactions with matter. In contrast, electron-flavored neutrinos

(anti-neutrinos) interact with matter to produce electrons (positrons) and decouple at a larger radius. Hence, the neutrino sphere of ν_x is smaller than that of ν_e and $\bar{\nu}_e$.

6.3.3 Flux calculation and neutrino oscillation

Here we discuss the methodology used in the analysis.

Flux Calculation: Figure 6.6 shows the luminosity, $L_\nu(t)$, and average energy, $\langle E_\nu(t) \rangle$, for various neutrino flavors over time in the Garching simulation. The flux of these neutrinos at the source is assumed to be quasi-thermal and modeled by the following expression [205]:

$$F_\nu^0(E_\nu, t) = L_\nu(t) \frac{(1 + \beta_\nu(t))^{1+\beta_\nu(t)}}{\Gamma(1 + \beta_\nu(t))} \times \frac{E_\nu^{\beta_\nu(t)}}{(\langle E_\nu(t) \rangle)^{\beta_\nu(t)+2}} \times \exp\left[-(\beta_\nu(t) + 1) \frac{E_\nu}{\langle E_\nu(t) \rangle} \right], \tag{6.1}$$

where ν represents ν_e, $\bar{\nu}_e$, ν_x, and $\beta_\nu(t)$ is the energy-shape parameter given by [206]

$$\beta_\nu(t) = \frac{2(\langle E_\nu(t) \rangle)^2 - \langle E_\nu(t)^2 \rangle}{\langle E_\nu(t)^2 \rangle - (\langle E_\nu(t) \rangle)^2} . \tag{6.2}$$

Neutrino Oscillation: Neutrinos produced in CCSN undergo two flavor conversion processes during their propagation from the dense medium to the outer layer of the collapsed star. Collective oscillation, influenced by interactions among neutrinos, is significant within a radius of $\mathcal{O}(10^3)$ km, while MSW oscillation becomes pronounced at around $\mathcal{O}(10^4)$ km. These two processes operate independently of each other [204]. Collective oscillations in iron-core SNe are suppressed due to trajectory-dependent multi-angle effects associated with dense matter [207–209], especially during the early stages after the core bounce. Recent studies, however, suggest that self-induced neutrino flavor conversion is possible in the SN core [210], equalizing flavor ratios and potentially masking MSW oscillation effects. Thus, the detected neutrino fluxes may exhibit the combined impact of MSW and collective oscillations, depending on the specific flavor conversion scenario. Since these processes occur at different length scales, their effects can be independently computed for the oscillated neutrino fluxes. Given the fluxes of different flavors at production ($F_{\nu_e}^0$, $F_{\bar{\nu}_e}^0$, and $F_{\nu_x}^0$) in Eq. 6.1, the oscillated neutrino fluxes (F_{ν_e}, $F_{\bar{\nu}_e}$, and F_{ν_x}) can be obtained using the MSW prescription as follows [204, 211, 212]:

- **Normal Ordering (NO)**

$$F_{\nu_e} = F_{\nu_x}^0 \, , \tag{6.3}$$

$$F_{\bar{\nu}_e} = \cos^2 \theta_{12} F_{\bar{\nu}_e}^0 + \sin^2 \theta_{12} F_{\nu_x}^0 \, . \tag{6.4}$$

- **Inverted Ordering (IO)**

$$F_{\nu_e} = \sin^2 \theta_{12} F_{\nu_e}^0 + \cos^2 \theta_{12} F_{\nu_x}^0 \, , \tag{6.5}$$

$$F_{\bar{\nu}_e} = F_{\nu_x}^0 \, . \tag{6.6}$$

The mixing angle θ_{12} is given by $\sin^2 \theta_{12} = 0.31$. The fluxes of the heavy lepton flavor neutrinos (ν_x) can be determined by the relations $F_{\nu_e} + 2F_{\nu_x} = F_{\nu_e}^0 + 2F_{\nu_x}^0$ and $F_{\bar{\nu}_e} + 2F_{\bar{\nu}_x} = F_{\bar{\nu}_e}^0 + 2F_{\bar{\nu}_x}^0$ [211]. To calculate neutrino events from a core-collapse supernova (CCSN) at the previously mentioned detectors, we utilize the publicly available code "SNOwGLoBES: SuperNova Observatories with GLoBES" [213]. This software is specifically designed for generating supernova neutrino events in various detectors, including water Cherenkov, scintillator, liquid argon, and lead. The code computes interaction rates and smeared rates for each interaction channel in a given detector as a function of energy. GLoBES library is employed by the code to calculate event rates for each channel in a detector. It's important to note that SNOwGLoBES does not incorporate neutrino oscillations. We conduct the flavor conversion calculations independently of SNOwGLoBES, employing the equations outlined in the previous section. Here, un-oscillated neutrino fluxes at the source are obtained using equation 6.1. Subsequently, these oscillated neutrino fluxes serve as input for SNOwGLoBES. In the sections that follow, we present and analyze the results obtained with SNOwGLoBES for the detectors exploring potential implications on neutrino mass ordering.

As previously discussed, supernova neutrinos, undergoing MSW oscillation, may reveal signatures related to neutrino mass ordering, such as the "prompt ν_e burst" and the "faster rise of ν_x than $\bar{\nu}_e$." These distinctive features can potentially be observed in upcoming galactic supernovae using detectors like HK, DUNE, and JUNO. Given the sensitivity of these detectors to ν_e and $\bar{\nu}_e$, we calculate the anticipated events of these flavors from a supernova at a distance of 10 kpc. The fluxes of these neutrinos are contingent on the specific supernova simulation and the progenitor's mass. Consequently, we explore potential implications for detection prospects across various simulation models.

6.3.4 Impact on Neutrino mass ordering

In this section we discuss the capability of the experiment towards resolving the neutrino mass ordering for both neutrinization and rise time phase.

Neutronization burst phase: The flux of ν_e from a supernova exhibits distinct patterns for the two mass ordering scenarios (NO and IO), as indicated by equations 6.3 and 6.5. The anticipated number of ν_e events over time for these scenarios at DUNE (left) and HK (right) is presented in the top panel of figure 6.7. These plots, based on the Garching simulation of a 12 M$_\odot$ progenitor at a supernova distance of 10 kpc, reveal similar event patterns for both detectors. However, DUNE is capable of detecting more ν_e events than HK due to its detection channel relying on the charge current interactions with argon. In contrast, HK can detect ν_e through elastic scattering on electrons and charge/neutral current interactions with oxygen, with elastic scattering dominating up to 20 MeV. Since the supernova neutrino spectra peak around 10-15 MeV and decrease rapidly beyond 20 MeV, the primary detection channel for ν_e at HK is elastic scattering with electrons. Despite this, the cross-section for ν_e scattering on electrons is significantly smaller than that of charge current interaction in DUNE, resulting in a larger number of events at DUNE. Both panels demonstrate distinct event patterns for the two mass ordering scenarios (NO and IO). The IO spectra exhibit a prominent peak around 5-10 ms, while no peak is observed in the NO spectra, aligning with the formulations in equations 6.3 and 6.5. This distinction arises from the ν_e flux for IO, which is a combination of the unoscillated ν_e (31%) and ν_x (69%) fluxes. The unoscillated ν_e flux experiences a significant peak during the neutronization burst, resulting in the conspicuous appearance of this large peak at both detectors, serving as a clear indicator of the mass ordering. The bottom panel of figure 6.7 displays the number of ν_e events at DUNE (left) and HK (right) for various progenitor masses in the Garching simulation, assuming a supernova distance of 10 kpc. The neutronization burst peak is evident in all models for IO and absent for NO, underscoring its uniqueness independent of the progenitor mass. Thus, all models exhibit a clear distinction between NO and IO in both detectors. However, the spectra for a particular mass ordering (NO or IO) across different progenitor masses closely resemble each other. Consequently, DUNE and HK may not precisely determine the progenitor mass.

Rise time phase: Early ν_e emission (around 20 ms) from a supernova explosion has been identified as a potential means to determine neutrino mass ordering at DUNE and
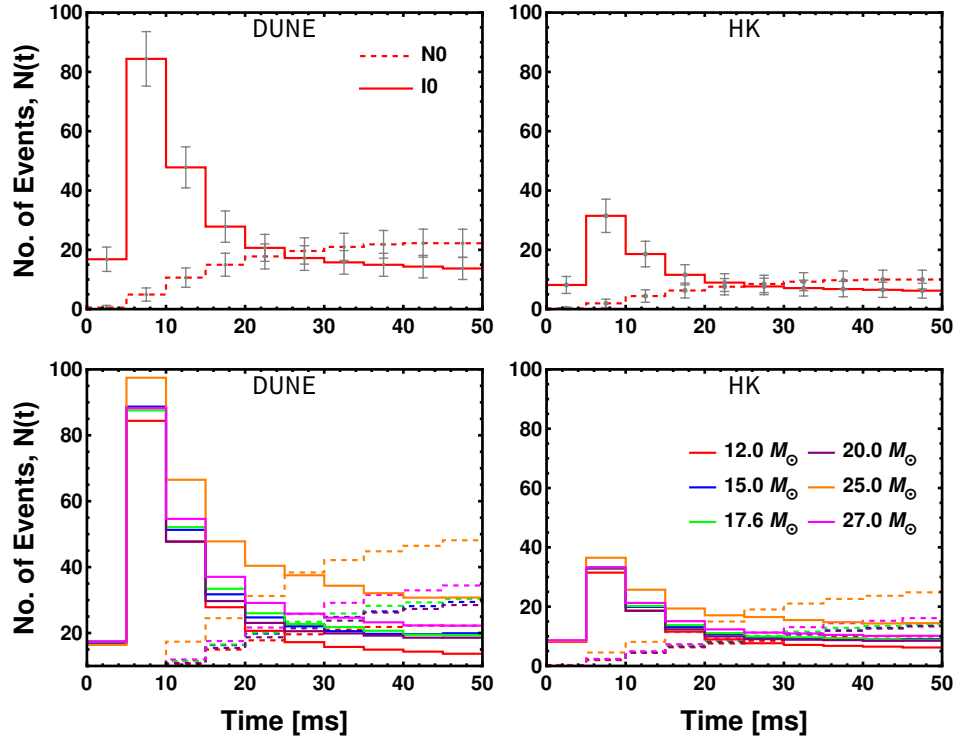
FIGURE 6.7: *Top:* Expected number of ν_e events at DUNE (left) and HK (right) for a progenitor of 12 $M_\odot$ of Garching simulation. The Poisson standard deviation of the events is shown by the error bars. *Bottom:* Expected number of ν_e events at DUNE (left) and HK (right) for different progenitor masses of Garching's simulation.

HK. During this phase, other neutrino species are suppressed due to high electron degeneracy. Upon the decline of this degeneracy during deleptonization, rapid production of $\bar{\nu}_e$ and ν_x ensues. The luminosity of ν_x rises more rapidly than that of $\bar{\nu}_e$. Depending on the mass ordering, this characteristic of the ν_x flux may significantly influence the MSW oscillated flux of $\bar{\nu}_e$, as demonstrated in Eqs. 6.4 and 6.6. Thus, the oscillated $\bar{\nu}_e$ flux in the IO case exhibits a faster rise than that in the NO case. Detecting this oscillated $\bar{\nu}_e$ flux provides a means to probe the true mass ordering scenario. Given that detectors like HK and JUNO are sensitive to $\bar{\nu}_e$, we explore the possibility of discerning neutrino mass ordering at these detectors from a future supernova at 10 kpc using Garching simulations. For this purpose, we compute the expected number of $\bar{\nu}_e$ events at these detectors over time with a resolution of 5 ms for different supernova progenitor models using SNOwGLoBES. The top panel of figure 6.8 illustrates the expected $\bar{\nu}_e$ events at HK (left) and JUNO (right) for a supernova with a 12$M_\odot$ progenitor from Garching's simulation. Continuous and dashed lines represent NO and IO, respectively. Both detectors employ the IBD detection channel. The plots clearly demonstrate that HK is capable of detecting a much larger number of events (approximately an order of magnitude) than JUNO, owing to its larger size. The spectra of $\bar{\nu}_e$ for the IO case rise

faster than those for the NO case in both detectors. As discussed earlier, this behavior arises from the faster rise of the unoscillated νx flux compared to the unoscillated $\bar{\nu}_e$ flux. In the NO case, the $\bar{\nu}e$ spectra consist of 31% ν_x and 69% $\bar{\nu}_e$ unoscillated flux, whereas in the IO case, $\bar{\nu}_e$ is solely composed of the unoscillated ν_x flux. The crossing between NO and IO spectra around 60 ms is attributed to the increased efficiency of $\bar{\nu}_e$ production with time due to the decreasing electron degeneracy, with processes like positron capture and electron-positron annihilation contributing significantly. Nevertheless, it is worth noting that the NO and IO cases exhibit a clear separation, making it feasible to distinguish them at these detectors. The middle panel of figure 6.8 displays the expected number of $\bar{\nu}_e$ events at HK (left) and DUNE (right) for different progenitor models in Garching's simulation (12M$_\odot$–red, 15 M$_\odot$–blue, 17.6 M$_\odot$–green, 20 M$_\odot$–purple, 25 M$_\odot$–orange, 27 M$_\odot$–magenta). The NO and IO cases are represented by dashed and continuous lines, respectively. Each progenitor model exhibits a clear distinction between NO and IO cases, similar to the 12 M$_\odot$ case discussed earlier. However, the separation between the NO case of a particular progenitor mass and the IO case of another progenitor mass is not evident in these plots and requires further analysis.

While the mass ordering scenarios appear distinguishable within a specific progenitor model, the degree of separability remains unclear. Moreover, it is crucial to assess the distinguishability of these oscillation scenarios across different progenitor models, such as determining if the NO case of a 12 M$_\odot$ model is distinguishable from the IO case of a 15 M$_\odot$ model. To gain a better understanding of these issues, we delve deeper into the characteristics of neutrino emission. As previously discussed in figure 6.6, the ν_x luminosity rises faster than that of $\bar{\nu}_e$ and peaks at around 20 ms, with both saturating around 100 ms. These characteristic time scales could prove useful for discerning mass ordering signals in the oscillated flux, specifically $\bar{\nu}_e$ in detectors. To this end, we define the following ratio:

$$\text{Ratio} = \frac{\text{Cumulative events at } t_1}{\text{Cumulative events at } t_2}, \tag{6.7}$$

where, $t_1 < t_2$. We take $t_1 = 20$ ms, $t_2 = 100$ ms as discussed above. In figure 6.9, we plot this ratio as a function of cumulative events at t_2 for different progenitor models in Garching's simulations. The left panel corresponds to HK, while the right panel corresponds to JUNO. The top panel displays NO (red) and IO (blue) scenarios, while the bottom panel includes the FE case as well. Error bars represent propagated errors from 1σ Poisson uncertainty in the events. Notably, the errors for JUNO are larger than those for HK, given the smaller number of events detected by JUNO. In HK, mass ordering scenarios, NO and IO, are well separable for both simulations within
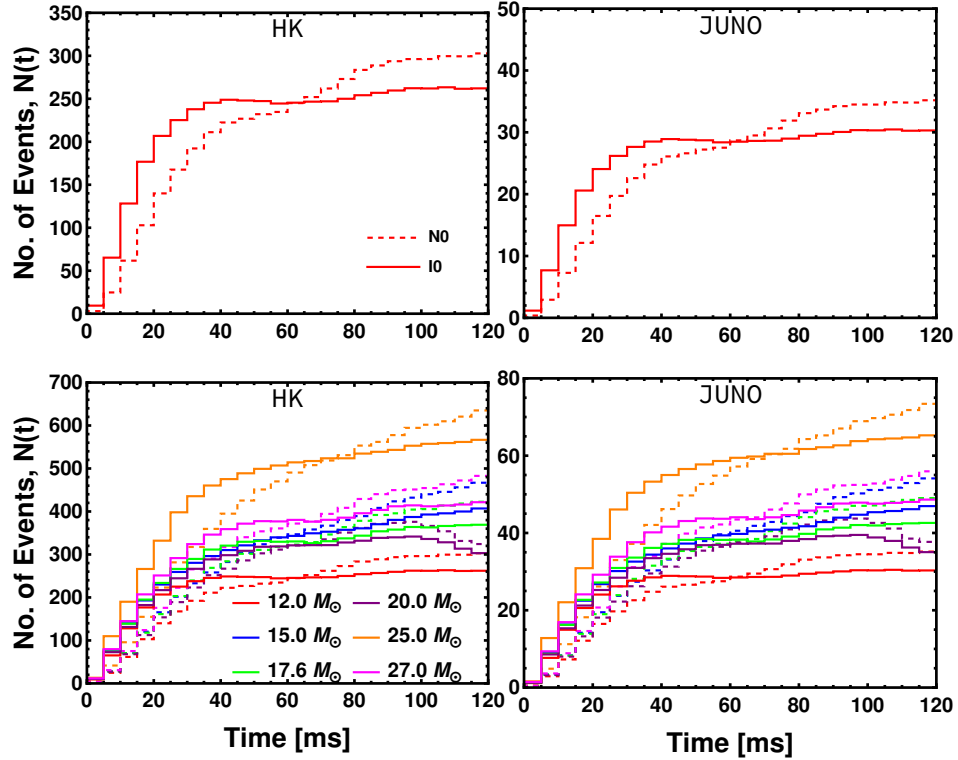
FIGURE 6.8: *Top:* Expected number of $\bar{\nu}_e$ events at HK (left) and JUNO (right) in different mass ordering scenarios (NO and IO) for a progenitor of 12 $M_\odot$. *Middle:* Expected number of $\bar{\nu}_e$ events at HK (left) and JUNO (right) in different mass ordering scenarios (NO and IO) for different progenitor masses. *Bottom:* Expected number of $\bar{\nu}_e$ events at HK (left) and JUNO (right) in the FE scenario (gray) along with the different mass orderings (NO and IO) for a progenitor of 12 $M_\odot$.

a specific progenitor mass model or across different models. However, discrimination is less effective in JUNO due to larger uncertainties.
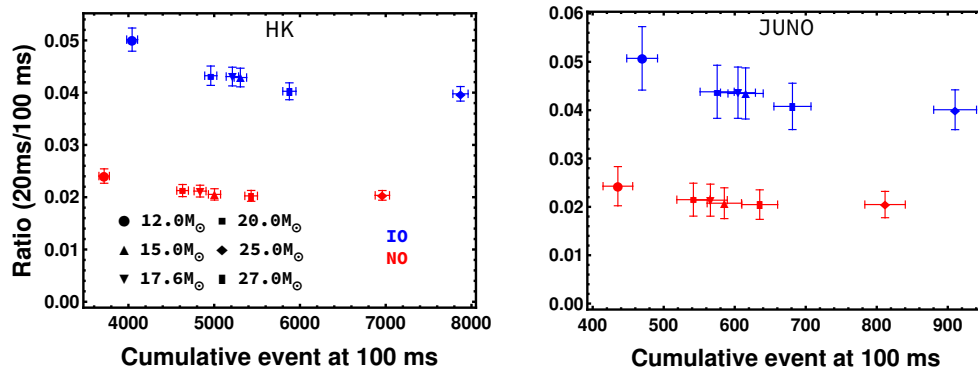

FIGURE 6.9: Ratio of cumulative events at 20 ms to cumulative events 100ms vs cumulative events at 100ms for HK (left) and JUNO (right) for Garching's simulation. The top panel shows the two mass ordering scenarios (NO and IO) whereas bottom panel includes the FE case as well.

A core-collapse supernova explosion releases 99% of the progenitor star's gravitational energy in the form of neutrinos, resulting in the emission of a substantial number of MeV neutrinos (approximately ($\sim \mathcal{O}(10^{56})$)). This neutrino emission occurs in three distinct phases: the neutronisation burst, accretion, and cooling, each associated with different physical processes. Interestingly, neutrinos from the neutronisation burst and accretion phases carry unique signatures of neutrino masses and mixing. In particular, for electron antineutrino detectors, the rapid increase of heavy lepton flavour antineutrinos at the supernova core can lead to distinct temporal signal characteristics for various mixing scenarios. Similarly, the neutronization burst phase, characterized by the absence of all other flavours except electron neutrinos, is sensitive to the mixing scenarios. This sensitivity aids in resolving the long-standing problem of neutrino mass ordering, distinguishing between normal mass ordering and inverted mass ordering. In this study, we explore the potential of determining the neutrino mass ordering using Hyper-Kamiokande (HK), JUNO (for the accretion phase), and DUNE (for the neutronisation burst phase) for different supernova models at galactic distances (approximately 10 kpc). Our analysis reveals that all these detectors exhibit the capability to distinguish between the two scenarios, normal ordering and inverted ordering, with high statistical significance across most supernova models.

6.4   Detector Instrumentation: Leak test of RPC

In the realm of instrumentation, our primary emphasis has centered around the study of the Resistive Plate Chamber (RPC) detector and the scrutiny of its efficiency for potential integration into experiments. Our efforts have predominantly involved the fabrication and subsequent testing of RPCs. The key merits associated with RPCs include their excellent particle detection efficiency, good spatial resolution, extensive coverage area, and cost-effectiveness. The successful execution of an experiment hinges on the uninterrupted and reliable operation of each RPC, with no discernible signs of aging over its entire operational lifespan. To ensure the success of an experiment, it becomes important to subject the RPC glass gaps to comprehensive leak tests, a practice integral both during the production phase and throughout the operational duration. This meticulous testing process is crucial for the seamless functioning of the experiment, as it guarantees the integrity and longevity of the RPCs, thereby contributing to the overall success of the experimental endeavor.

In the following, we discuss the details of the INO's ICAL experiment where RPCs will be used as active detector elements. We then discuss the details of RPC fabrication and its working principle. Finally, we discuss the results of our leak test study.

6.4.1   India-based Neutrino Observatory:

India-based Neutrino Observatory (INO) [214] is a proposed underground neutrino experiment facility which will house a 50 kt Iron Calorimeter (ICAL) detector and will be located in Pottipuram in Bodi West hills of Theni District of Tamil Nadu, India. The facility will consist of an underground cavern with approximately minimum rock cover of ~ 1 km in all directions. The magnetized ICAL detector of INO facility would be able to distinguish neutrinos and antineutrinos separately in the multi-GeV range of energies covering baselines over a wide range of 10 to 10^4 km. Due to the presence of a magnetic field of 1.5 Tesla [215], ICAL would be able to distinguish between μ^- and μ^+ events separately. The ICAL has a very high resolution of direction and energy for upward-going muons in the energy range of 1 to 10 GeV, which enables ICAL to observe the matter effect felt by neutrinos. The ICAL detector is designed in the form of three identical modules of dimensions 16 m $\times$ 16 m $\times$ 14.5 m placed side by side. The detector modules are made up of 151 horizontal layers of 5.6 cm thick low carbon iron plates with 4 cm gap between them to place the Resistive Plate Chambers (RPCs). RPCs are basically parallel plate detectors made up of very high resistive materials like glass or Bakelite. The main benefits of the RPCs are its very good detection efficiency,

good spatial resolution, wide-area coverage and low production cost. The INO-ICAL detector specifications and other details are listed in table 6.1.

ICAL	
No. of modules	3
Module dimension	16 m × 16 m × 14.5 m
Detector dimension	48 m × 16 m × 14.5 m
No. of layers	151
Iron plate thickness	5.6 cm
Gap for RPC trays	4.0 cm
Magnetic field	1.5 Tesla
RPC	
RPC unit dimension	2 m × 2 m
Readout strip width	3 cm
No. of RPC units/Layer/Module	64
Total no. of RPC units	$\sim 28,800$
No. of electronic readout channels	3.9×10^6

TABLE 6.1: Specifications of the INO ICAL detector.

6.4.2 Resistive Plate Chamber

The Resistive Plate Chamber (RPC) emerged in 1981 through the work of R. Santonico and R. Cardarelli [216]. It served as a practical substitute for the highly localized discharge spark counters, which ultimately accomplished a time resolution of 25 ps. The RPC operates on a principle similar to Pestov's Planar Spark Chamber. Nonetheless, it underwent significant simplifications in its implementation. These included the elimination of high-pressure gas, reduced demands for mechanical precision, and the adoption of plastic materials instead of glass. This resultant detector was inherently immune to detrimental discharges due to its design and yielded a time resolution on the order of 1 ns. These combined advantages rendered RPCs appealing for a broader array of contemporary experiments. Notably, due to cost considerations, they took the place

of plastic scintillators in scenarios requiring extensive detection areas within low-count rate environments.

An RPC refers to a type of particle detector that employs a constant and evenly distributed electric field generated by two parallel electrode plates. At least one of these plates is composed of a material with high bulk resistivity. The space between the electrodes allows a gas mixture with a strong ability to absorb ultraviolet light to flow through. When a charged particle traverses the chamber and ionizes the gas, free charge carriers are introduced into the gap. These charge carriers then initiate chains of electron avalanches in the applied electric field, leading to a discharge. Due to the electrodes' high resistivity, the electric field experiences a sudden reduction in a localized region surrounding the point where the discharge originated. Consequently, the discharge is prevented from spreading throughout the entire gas volume, leaving the counter's sensitivity unaffected beyond this limited area. Additionally, the gas mixture's capability to absorb ultraviolet light ensures that the photons produced by the discharge cannot propagate within the gas. This effectively eliminates the possibility of secondary discharges originating from other locations within the detector. As the number of electrons generated by the discharge continues to grow, it induces a current on external strip electrodes. RPCs exhibit significantly improved time resolution compared to wire chambers or limited streamer tubes. This advantage comes from the uniform electric field, in contrast to the 1/r field found in wire chambers, which introduces substantial temporal fluctuations due to electron drift motion. Recent developments involve advanced versions of RPCs, wherein exceptionally flat electrodes made of semi-conducting glass and high-pressure gas are employed. These sophisticated detectors offer time resolutions that surpass even those achievable by scintillators and fast photomultipliers.

A depiction of the RPC detector setup can be observed in figure 6.10. The configuration involves a gas mixture held between two flat electrodes (constructed from glass in this instance) characterized by a bulk resistivity of approximately 10^{12} Ω cm. Separating the gas are cylindrical polycarbonate spacers, which possess a higher bulk resistivity exceeding 10^{13} Ω cm. These spacers are employed to uphold the gas gap. The chamber's lateral sections are carefully sealed by affixing specific spacers. Furthermore, inlets and outlets are connected to facilitate a continuous flow of gas. The external surfaces of the two electrodes are coated with conductive graphite layers. These electrodes are then connected to a high-voltage power supply to sustain a uniform and constant electric field (around 5 kV/mm) across the gas gap.
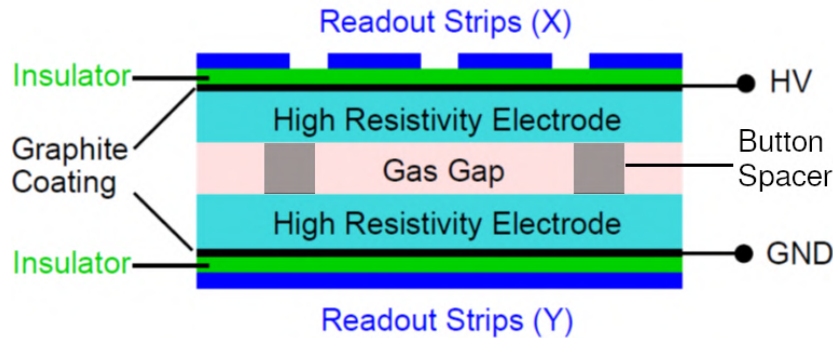
FIGURE 6.10: Schematic of a Resistive Plate Chamber detector.

6.4.3 Leak test of RPC

The ICAL detector is set to utilize around 28,800 RPCs and is designed for a 20-year operational lifespan. In order to ensure the experiment's success, it is important that each RPC operates without displaying notable signs of aging throughout its entire operational duration. Consequently, a series of tests are conducted both during and following the production process. While the ICAL detector is actively operating, it relies on circulating more than 200,000 liters of gas mixtures through its 28,800 RPCs. To facilitate this process, a closed-loop gas system has been designed with the primary goal of efficiently mixing and recirculating the gas mixture to minimize gas wastage and thus reduce operational costs. Any leakage of the gas mixture from this closed-loop system would lead to increased operational expenses. Additionally, if the outside atmosphere were to infiltrate the system, it could contaminate the gas mixture with water vapor and oxygen, potentially causing damage to the RPC [217, 218]. Notably, the presence of fluorine in the RPC gas mixture can react with water vapor to produce hydrofluoric acid, which can harm the inner surfaces of the glass electrodes. Oxygen, being electron-affinitive, can also impact the detector's gain and performance. Consequently, it is imperative to conduct thorough leak tests on all glass gaps both during production and throughout operation for the aforementioned reasons.

Figure 6.11 illustrates the configuration of a typical leak test setup. In this procedure, the RPC undergoes pressurization to a level 45 mmWC higher than atmospheric pressure before being completely sealed. Subsequently, the pressure within the RPC is meticulously monitored over an extended duration. It's important to note that a conventional manometer measures the differential pressure. The techniques for calculating leak rates via a conventional manometer are applicable only under the condition that both the test subject's volume and the ambient pressure remain constant. However, in the case of an RPC gas gap, both of these parameters are significantly influenced
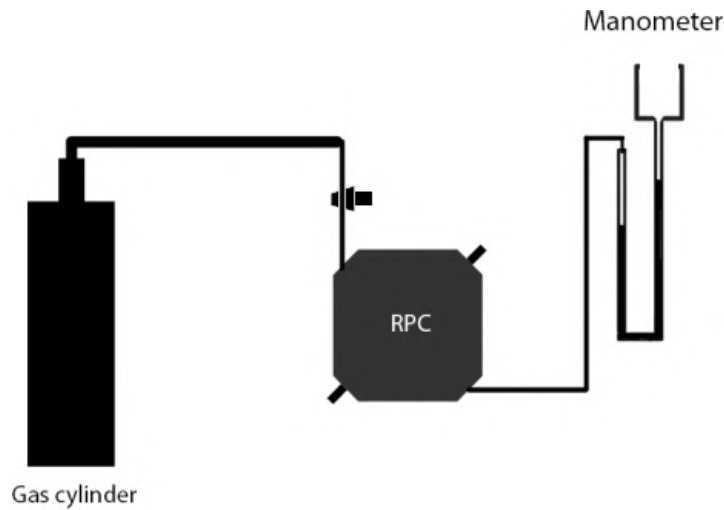
FIGURE 6.11: Schematics of a typical leak test setup.

by variations in ambient pressure and temperature, which are subject to fluctuations due to solar atmospheric tides and changing weather conditions. Consequently, when measuring pressure using a conventional manometer over an extended period, significant pressure variations are observed. In such circumstances, the detection of very minor leaks in the RPC becomes exceedingly challenging, and obtaining an accurate quantitative assessment of the leak rate from pressure measurements becomes unfeasible [219].

In accordance with Poiseuille's law [220], equation 6.8 defines the laminar flow rate of a fluid through a leak path:

$$\text{Flow Rate} = \text{Leak Constant} \times \text{Effective Pressure Difference} \tag{6.8}$$

Here, the *Leak Constant* relies on the nature of the leakage path (such as cracks or holes) and the viscosity of the gas mixture. It serves as a measure of the system's leakage.

6.4.4 The Experimental Setup

The experimental setup schematics are depicted in figure 6.13. In this configuration, instead of employing the traditional manometer to measure the differential pressure, the absolute pressure and temperature within the gas gap are measured using the BMP180 sensor module (Figure 6.12) manufactured by BOSCH [221]. This piezo-resistive sensor has an accuracy of 0.7 mmWC for pressure measurements and 0.05 °C for temperature measurements. Additionally, the sensor can capture data samples at intervals as short as 76 ms.

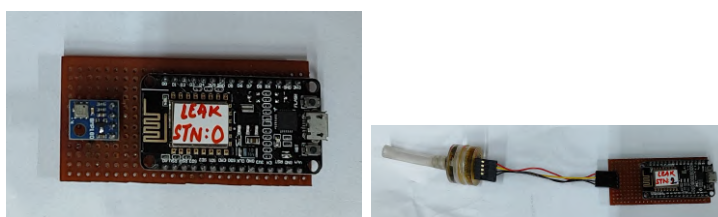FIGURE 6.12: BMP180 sensor to measure pressure and temperature.

FIGURE 6.13: Leaq test module to measure ambient (left) and RPC (right) pressure and temperature.

The leak test module, as shown in figure 6.13, is designed to record pressure and temperature data for ambient and RPC gaps. A Raspberry Pi v2 B unit [222], is responsible for retrieving and storing the data on its onboard memory. Each module features two bus ports, enabling the daisy-chaining of multiple leak test modules, all controllable from a single Pi unit. It's worth noting that data from the BMP180s can also be wirelessly acquired using microcontrollers equipped with WiFi modules, such as the NodeMCU module [223]. These modules utilize the WiFi network within the premises to transmit data to a computer on the same network, eliminating the need for wired communication buses and multiple Pi units. In our present configuration, we continuously collect pressure and temperature data from individual sensors at fixed 3-second intervals. The resulting dataset for a gas gap encompasses readings of ambient pressure and temperature, gas gap pressure and temperature, along with corresponding timestamps for each measurement. The following sections outline the approach for assessing the extent of leakage based on these recorded measurements.

6.4.5 Volume correction due to bottom pop ups

The structural integrity of the RPC relies on the secure attachment of buttons, which are essential components to maintain a gap between the glass electrodes. However, there have been instances where the adhesive connecting these buttons to the glass
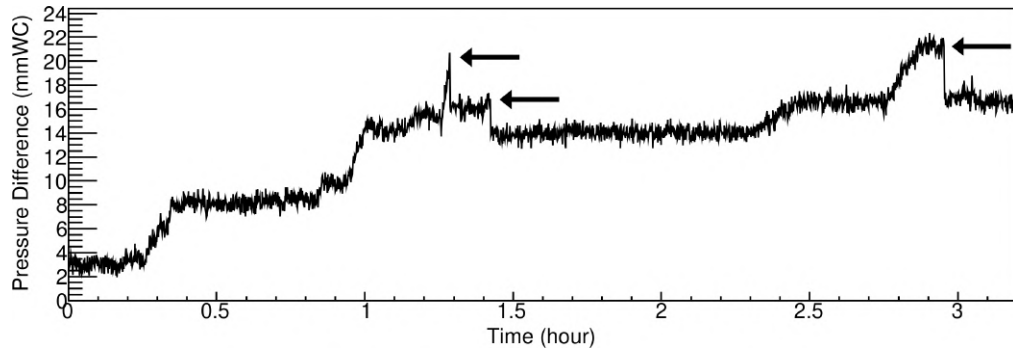
FIGURE 6.14: The variation of pressure difference over time with three button pop-ups. Image taken from [23] for reference.

plates failed to withstand pressure, leading to the detachment of the buttons from the glass plates. This occurrence, hereafter referred to as a 'button pop-up', not only weakens the RPC structure but also widens the gap between the glass plates during detector operations. This increased gap reduces the effective electric field, resulting in a weaker signal. For an RPC to function correctly, it is crucial that the glue holding the buttons to the glass plates remains undamaged under pressure. If any button becomes detached, the corresponding gas gap will not be able to withstand pressure effectively, and this problem may propagate as the adhesive for other buttons may also weaken over time. Therefore, detecting 'button pop-up' events during leak tests is essential. Each 'button pop-up' event increases the volume of the RPC gap, subsequently decreasing the pressure within the gap. As a result, the pressure difference between the interior and exterior of the gap diminishes. This phenomenon manifests as a sudden drop in the pressure difference when observing the pressure difference over time, as illustrated in figure 6.14. The figure clearly highlights three 'button pop-up' events (indicated by arrows) in this RPC. These events significantly and rapidly reduce the pressure difference. Traditional manometers are incapable of detecting such events unless pressure is continuously recorded using a precise differential pressure sensor.

6.4.6 Calculation of leak rate

The temporal profiles of gas gap temperature are shown in the top panel of figure 6.15 and pressure within the glass gap and the atmosphere are shown in the middle panel of figure 6.15. Notably, the gap pressure closely mirrors the atmospheric pressure, indicating a correlation between gap volume and atmospheric pressure. To ascertain the gas quantity (n) within a chamber of volume V at time t, the Ideal Gas Law is employed as follows,

$$n_{\mathrm{rpc}jt} = \frac{P_{\mathrm{rpc}jt}V_{\mathrm{rpc}jt}}{RT_{\mathrm{rpc}jt}} \qquad (6.9)$$

Here, R represents the ideal gas constant, valued at 8.314 J·mole^{-1}·K^{-1}. The gas gap's approximate volume, derived from its dimensions, is around 6.3 liters. Using this data, the gas quantity inside the gap is computed with equation 6.9, as illustrated in figure 6.16. The instantaneous leak rate of the gap is quantified by the slope of this graph.

To determine the absolute leak rate, Poiseuille's equation for compressible fluids is applied [220]. Poiseuille's Leak Rate equation for compressible fluids, as shown below, is used for this purpose:

$$\frac{\mathrm{d}n_{\mathrm{rpc}}}{\mathrm{d}t}\bigg|_t = \mathrm{C}_{\mathrm{Leak}} \times \left(\frac{P_{\mathrm{rpc}jt}^2 - P_{\mathrm{atm}jt}^2}{2P_{\mathrm{rpc}jt}} \right) \qquad (6.10)$$

The parameter $\mathrm{C}_{\mathrm{Leak}}$ characterizes the leakage in the system and depends on the type of leakage path (e.g., crack or hole) and the viscosity of the gas mixture. The viscosity of the gas is assumed constant within small temperature variations during the testing period, but variations in viscosity should be considered for larger temperature changes. Figure 6.17 displays the calculated leak rate $\left(\frac{\mathrm{d}n_{\mathrm{rpc}}}{\mathrm{d}t} \right)$ as a function of the effective pressure difference $\left(\frac{P_{\mathrm{rpc}}^2 - P_{\mathrm{atm}}^2}{2P_{\mathrm{rpc}}} \right)$. According to equation 6.10, a straight line with a slope quantifying the system's leakage is expected, but the graph clearly deviates from this behavior.

Furthermore, the gas gap being tested is isolated from the inlet, which prevents any further gas from entering. However, despite this sealing, figure 6.16 illustrates an apparent increase in the gas volume inside the gap. This phenomenon can be attributed to variations in atmospheric pressure and room temperature, resulting in changes in the gas gap's volume. Unfortunately, the extent of this volume change remains unknown and cannot be directly measured. To account for this variability in volume, the gas gap's volume at time t can be approximated using the following equation,

$$V_{\mathrm{rpc}jt} = V_{\mathrm{rpc}} \left(1 - x_T \left(T_{\mathrm{rpc}jt} - T_{\mathrm{rpc}jt=0} \right) \right) \left(1 - x_P \left(P_{\mathrm{atm}jt} - P_{\mathrm{atm}jt=0} \right) \right) \qquad (6.11)$$

Here, $T_{\mathrm{rpc}jt=0}$ and $P_{\mathrm{atm}jt=0}$ correspond to the temperature and atmospheric pressure at the initial time $t = 0$, respectively. Notably, V_{rpc} is fixed at 6.3 liters. To address the assumption of linearity between volume changes and atmospheric pressure and temperature variations, two independent linear correction terms, denoted as x_P and x_T, are
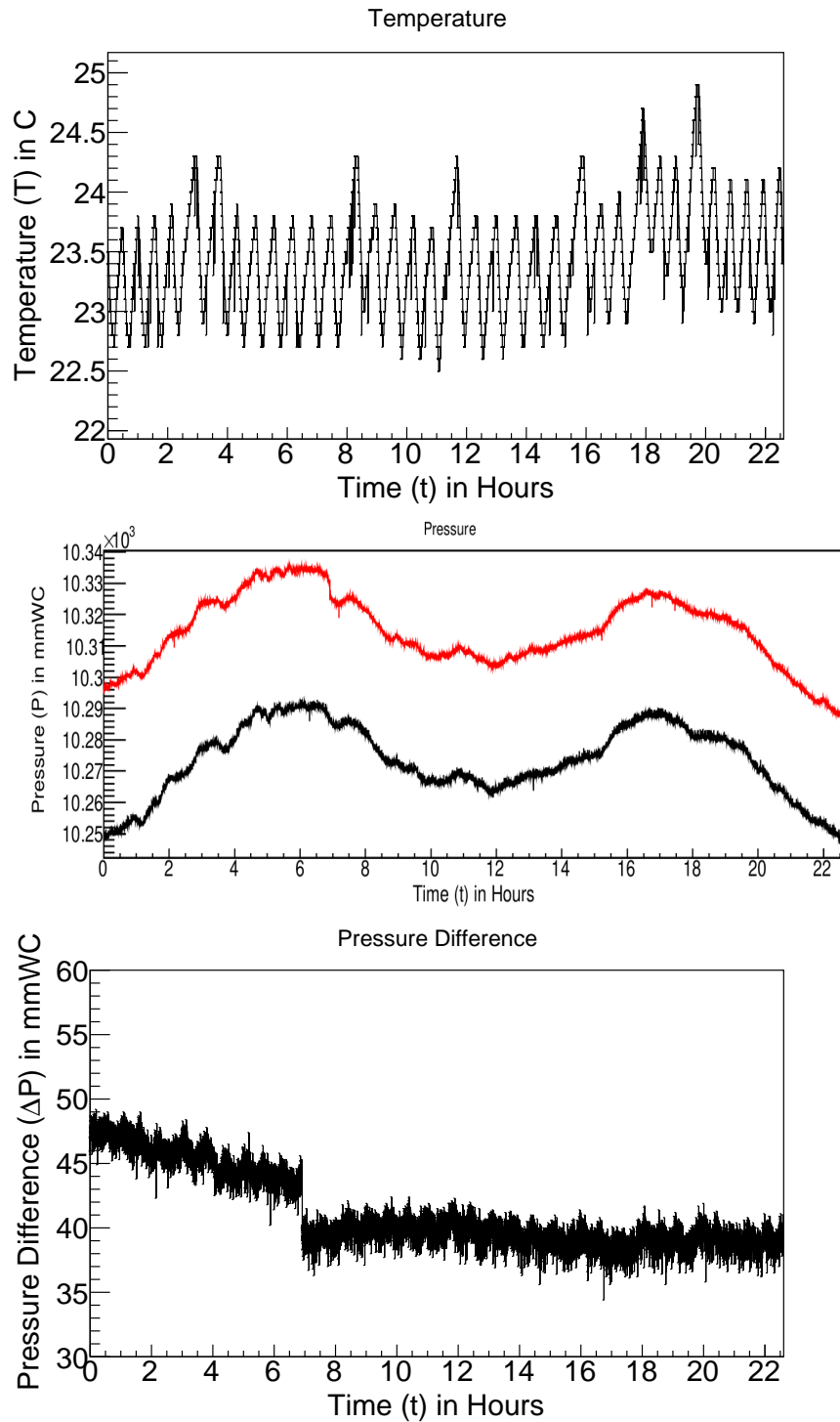
FIGURE 6.15: *Top-panel:* RPC temperature variation with time, *middle-panel:* Pressure variation of RPC (red) and atmosphere (black) with time, *bottom-panel:* pressure difference of RPC and atmosphere with time.

introduced. By employing the volume calculated in equation 6.11, the quantity n_{rpc} is expressed as follows,
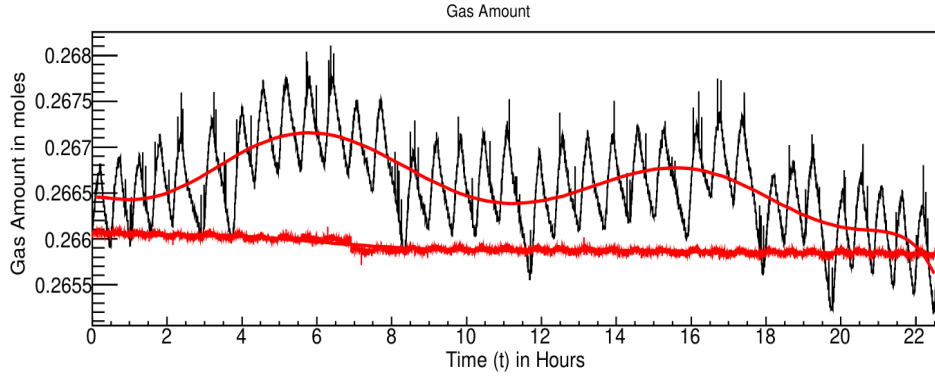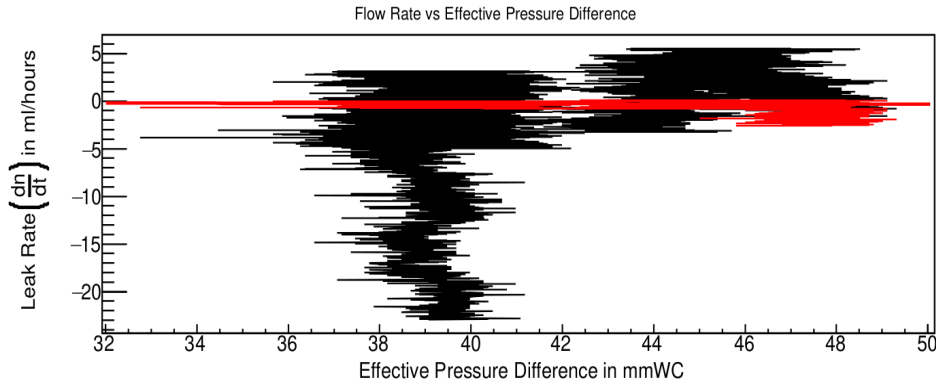
FIGURE 6.16: The variation of gas quantity within the RPC over time.

FIGURE 6.17: Leak rate $\left(\frac{\mathrm{d}n_{\mathrm{rpc}}}{\mathrm{d}t}\right)$ as a function of the effective pressure difference $\left(\frac{P_{\mathrm{rpc}}^2 - P_{\mathrm{atm}}^2}{2P_{\mathrm{rpc}}}\right)$.

$$n_{\mathrm{rpc}jt} = \left(\frac{V_{\mathrm{rpc}}}{R}\right) \left(\frac{P_{\mathrm{rpc}jt}}{T_{\mathrm{rpc}jt}}\right) \left(1 - x_T \left(T_{\mathrm{rpc}jt} - T_{\mathrm{rpc}jt=0}\right)\right) \left(1 - x_P \left(P_{\mathrm{atm}jt} - P_{\mathrm{atm}jt=0}\right)\right)$$

(6.12)

For various values of x_T and x_P, we compute n_{rpc} using equation 6.12 and represent it over time and for each combination of correction terms, we analyze the plot of n_{rpc} versus time to derive $\frac{\mathrm{d}n_{\mathrm{rpc}}}{\mathrm{d}t}$. The resultant graph of $\frac{\mathrm{d}n_{\mathrm{rpc}}}{\mathrm{d}t}$ against $\frac{P_{\mathrm{rpc}}^2 - P_{\mathrm{atm}}^2}{2P_{\mathrm{rpc}}}$ is then fitted with a linear regression, and we calculate χ^2/ndf. The minimum χ^2/ndf for a particular combination of x_T and x_P is obtained and to minimize uncertainties at this minimum χ^2/ndf, we iterate the procedure with subsequently narrower ranges of x_T and x_P to obtain the final values. The variation of gas quantity within the RPC gap, calculated with these correction factors over time, is depicted in figure 6.16. This comparison with the data observed before volume correction reveals no increase in gas quantity within the gap, indicating the successful application of the volume correction. The relationship between leak rate and effective pressure difference, shown in figure 6.17, exhibits a linear

behavior as expected from Poiseuille's equation. The value of C_{Leak} calculated from this analysis is:

$$C_{\text{Leak}} = -(6.698) \times 10^{-3} \, \text{ml} \, \text{hour}^{-1} \, \text{mmWC}^{-1}.$$

In this context, a negative C_{Leak} value signifies an inward leak, indicating that a constant pressure difference of $40 \, \text{mmWC}$ between the inside and outside of an RPC gap will result in a leakage of $6.43 \, \text{ml}$ of gas over a 24-hour period. The small magnitude of C_{Leak} suggests that this gap has a relatively minor leak.
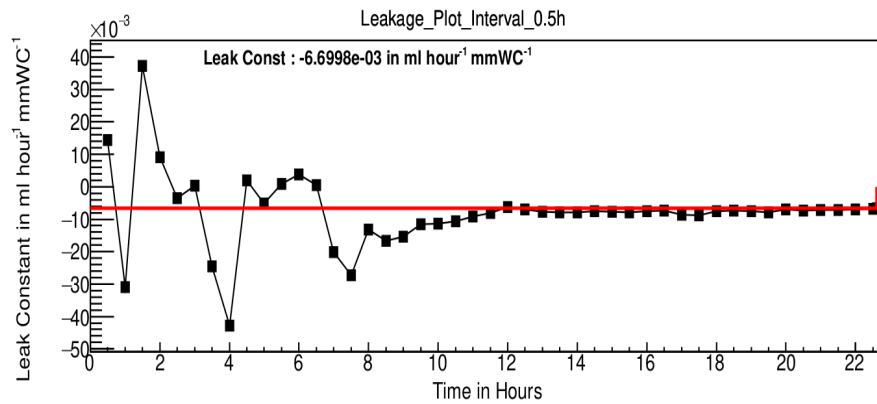

FIGURE 6.18: Leak rate as a function of time at an interval of 30 minutes.

The RPC gap was tested for approximately 23 hours. To determine the optimal or minimum duration required for a reliable leak rate calculation, the data was divided into various sets covering different time durations from the test's start time, and the C_{Leak} value was computed. In figure 6.18, the C_{Leak} value for varying time at an interval of 30 minutes is presented. For the RPC gap, it becomes evident that a minimum of 11-12 hours is necessary to estimate the leakage accurately. This method demands a substantial amount of data to fit the $\frac{\mathrm{d}n_{\text{rpc}}}{\mathrm{d}t}$ vs. $\frac{P_{\text{rpc}}^2 - P_{\text{atm}}^2}{2P_{\text{rpc}}}$ plots for reliable results. It should be noted that the minimal required test time depends on the leak quantity and the environmental conditions during the test.

6.5   Chapter Summary

In summary, this chapter encapsulates a comprehensive journey through my Ph.D. tenure, encapsulating the simulation work elucidating the detector sensitivity of the Hyper Kamiokande detector in diverse scenarios, including the challenging presence of radioactive backgrounds and the exploration of its capabilities in supernova neutrino detection. It also encompasses the instrumentation studies of my research, highlighting the fabrication and characterization of resistive plate chamber detectors, a pivotal component in the realm of particle physics experimentation.